Nanoscale visualization and multiscale mechanical implications of bound rubber interphases in rubber–carbon black nanocomposites†

Meng Qu,[a] Fei Deng,[a] Salmon M. Kalkhoran,[c] Andrew Gouldstone,[c] Agathe Robisson[*b] and Krystyn J. Van Vliet[*a]

The concept of a "bound rubber" phase extending over nanometre-scale distances from the interface of rubber-particle nanocomposites is generally accepted. However, the thickness and elastic properties of this interphase have not been confirmed by direct experimental observation. Here, we demonstrate the existence of bound rubber in hydrogenated nitrile butadiene rubber (HNBR)–carbon black composites, through direct visualization and measurement of elastic properties. Both macro- and nanoscale mechanical analyses show that the bound rubber exhibits an elastic modulus distinct from that of the rubber matrix and of the particles. Direct visualization of this bound rubber via scanning probe microscopy-based approaches requires detailed consideration of potential artifacts in contact-based analysis of viscoelastic nanocomposites. We quantify the magnitude of such contributions, and find that the bound rubber content decreases with increasing temperature, and that its stiffness exceeds that of the rubber matrix by approximately one order of magnitude. Further, the measured thickness and elastic moduli of this bound rubber are consistent with that predicted by our numerical model of a matrix–interphase–particle composite. Together, these experiments and model demonstrate that the elastic properties of nanocomposite interphases of less than 20 nm thickness can be interrogated directly.

1 Introduction

The mechanical optimization of elastomeric materials has been readily achieved via incorporation of carbon black (and other) nanoscale filler particles. Indeed, the rubber industry has used this modification extensively to increase abrasion resistance, elastic modulus and strength of elastomeric composites.[1,2] However, despite decades of such experimental and numerical studies,[1–9] the actual mechanisms by which carbon black modifies macroscale mechanical performance remain unresolved.[3–11] The dominant theory of this reinforcement posits a strong interaction at the particle–polymer interface, which then has effects on the mechanical behavior of the composites system.[5,10] The concept of "bound rubber" at the particle–elastomer interface has been put forth to describe such a strong interaction. As proposed initially by Stickney and Falb,[12] this bound rubber is a film that is stabilized around the particles via van der Waals interactions, and is thus resistant to dissolution in solvent. The proposed theory of this phenomenon is that the motion of macromolecular chains within the bound rubber phase is restricted by interaction with the filler particle surfaces, which would correlate with

increased resistance to mechanical deformation (i.e., stiffening) of the bound rubber layer as compared to the "free rubber" far from the particle interface.[12] As this interfacial region is of presumed finite width and distinct properties, the bound rubber can be considered as an interphase.

In practice, it has been historically difficult to characterize the existence of, and, by extension, the mechanical properties of bound rubber in such composites: the predicted thickness of bound rubber is in the nanometre range. To our knowledge, experimental efforts have been focused on indirect evidence of an interphase in the uncrosslinked state. For example, nuclear magnetic resonance (NMR) spectroscopy has suggested the existence of this interphase, in that chain mobility near the carbon black–rubber interfaces was less than that of the polymer matrix.[3,6,13,14] Litvinov and Steeman[6] measured T_2 relaxation spectra of ethylene propylene diene monomer rubber (EPDM) and bound rubber–coated carbon black fillers to imply significantly different EPDM rubber chain mobility. Berriot et al.[3] also demonstrated via NMR that topological constraints exist at a particle surface. Another indirect confirmation of this interphase is enabled by the unique property of bound rubber to reversibly form as a function of temperature, i.e., bound rubber content decreases at high temperature. This temperature effect has been studied on uncured rubber composites, wherein the weight of the composite is determined after exposure to a given temperature, followed by immersion in a solvent that dissolves any unbound rubber accessible at that temperature. Wolff et al.[11] thus showed a significant decrease in bound styrene–butadiene rubber content for temperatures exceeding 80 °C. Kida et al.[15] reported similar observations on polyisoprene/carbon black composites (45% decrease in apparent bound rubber from 25 °C

[a]Department of Materials Science and Engineering, Massachusetts Institute of Technology, 77 Massachusetts Avenue, Cambridge, MA, 02139, USA. E-mail: krystyn@mit.edu
[b]Schlumberger-Doll Research Center, 1 Hampshire Street, Cambridge, MA, 02139, USA. E-mail: agathe.robisson@gmail.com
[c]Department of Mechanical and Industrial Engineering, Northeastern University, Boston, MA, 02115, USA

to 110 °C). Robisson has also shown that macroscale elastic moduli of hydrogenated nitrile butadiene rubber (HNBR)–carbon black (CB) composites decreased with increasing temperature (for a given vol% carbon black), suggesting thermal depletion of the vol% of bound rubber interphase.[9,16] Each of these methods has been interpreted to predict either thickness (∼1 to 10 nm) or effective stiffness of the bound rubber interphase. However, the existence and elastic properties of this nanoscale interphase have not been demonstrated through direct visualization or mechanical characterization.

In this study, we explored the existence and elastic properties of bound rubber in cured HNBR/CB composites using scanning probe microscopy (SPM) analysis. To visualize this particle–elastomer interphase, we conducted atomic force microscopy (AFM) phase imaging at low (25 °C) and high (180 °C) temperatures at which changes in interphase thickness are anticipated. To determine the local elastic properties of this interfacial region, torsional harmonic AFM was conducted to obtain simultaneous stiffness and topography. These mechanical images demonstrate the existence of bound rubber and provide a first estimation of the elastic modulus and thickness of the interphase. We then applied a micromechanical analytical model to predict the thickness and stiffness of a putative interphase that would capture the macroscale elastic properties of this HNBR/CB composite. The strong correlation between these experimental measurements and independent analytical predictions supports the hypothesis that the nanoscale bound rubber interphase can be directly interrogated and quantified in cured rubber-particle nanocomposites.

2 Materials and methods

2.1 Materials

Processing details of these rubber–carbon black composites can be found elsewhere.[9] Briefly, hydrogenated nitrile butadiene rubber (HNBR, Lanxess) was mixed with carbon black fillers (N330, with an average particle radius of 13–15 nm,[17] Columbian Carbon Co.). Plasticizer was added for processing and the mixture was then sulfur cured. The reinforcing carbon black (CB) content ranged from 5 vol% to 28 vol% (Φ_{CB} = 0.05–0.28). Pure HNBR under otherwise identical processing served as control samples. The glass transition temperature of these composites was −26.5 ± 0.5 °C, measured via differential scanning calorimetry (DSC).[9] HNBR–CB composite samples were cut into 1 mm × 3 mm sections of ∼2 mm thickness and cryotomed (RMC MT-X cryo-ultramicrotome, Boeckeler Instruments, Tucson, AR) at −30 °C to obtain a smooth surface for AFM imaging. As N330 CB can exist as isolated particles and as aggregates, we will hereafter refer to both isolated and aggregated CB regions collectively as "CB particles." Upon increasing vol% CB, CB particles and aggregates can agglomerate, and we will refer to those hereafter as "CB agglomerates".

2.2 Relation of dynamic mechanical analysis (DMA) to AFM-enabled nanoindentation

Robisson has previously described and reported the macroscale dynamic mechanical analysis (DMA) of HNBR–CB composites of identical processing and vol% carbon black considered herein.[9] In that work, storage elastic moduli E' were measured under uniaxial tension at constant strain amplitude of 0.1% at a frequency of 1 Hz, over temperatures ranging from 35 °C to 180 °C.[9]

In order to relate the AFM-enabled nanoindentation analysis of the present samples, which were obtained at high-frequency (∼60 kHz), to the low frequency measurements used in the DMA of ref. 9, a time–temperature equivalence master curve was constructed. Here, the HNBR–5 vol% CB sample was tested via DMA (Q800, TA Instruments, New Castle, DE) at 0.1% strain amplitude between 0.1 Hz and 100 Hz, over temperatures near and above the glass transition temperature (−30, −27.5, −25, −22.5, −20, −17.5, −15, −12.5, −10 and 25 °C). The master curve was constructed via the Williams–Landau–Ferry (WLF) method, shifting measured E' data horizontally along the abscissa to overlap and form a continuous curve.[18] The WLF constants obtained by fitting this master curve are: $C_1 = 1.7$ and $C_2 = 66.2$ at 25 °C, and $C_1 = 11.7$ and $C_2 = 61.7$ at T_g (−26 °C for HNBR). This master curve gives access to a large frequency range of elastic moduli as needed in this study. Hereafter, E' obtained at the macroscale is assumed equivalent to the Young's elastic modulus at a specific frequency, and is denoted as E.

2.3 Scanning probe microscopy (SPM)-based imaging and force microscopy

The morphology of these composites was observed via atomic force microscopy (3D Molecular Force Probe, Asylum Research, Santa Barbara, CA). Silicon cantilevers (OMCL AC240TS-W2, Olympus, Tokyo) with nominal spring constant $k = 2$ N m^{-1} were used; the nominal probe radius and conical semi-apex angle were 10 nm and 35°, respectively. To probe the effects of temperature on bound rubber content, phase-lag images on the same area (1 μm × 1 μm images, scan rate of 1 Hz) were acquired by AC mode (tapping mode) at both room temperature (RT, ∼25 °C) and 180 °C. Sample heating was achieved via a Poly-Heater™ heating stage (Asylum Research, Santa Barbara, CA). Images were acquired after full stabilization of the desired temperature, as reported by a digital thermocouple. At least two images were acquired at each temperature; to ensure repeatability, sample temperature was cycled between RT and 180 °C for at least two full cycles of sample temperature. Image analysis was then conducted to calculate the interface width at the particle–rubber interface at different temperatures. Data quantifying particle diameter and interphase thickness are given as the mean, where the variation of the mean is standard deviation reflecting varied particle diameters; this variation is not standard error of measurement for a single particle diameter.

2.4 Torsional harmonic stiffness mapping and bound rubber characterization

2.4.1 Harmonic stiffness mapping. Morphology, phase and stiffness maps were obtained at the same scan with the torsional harmonic imaging technique. These experiments were conducted using a modified commercial AFM system (Multimode™, Veeco Instruments Inc., Santa Barbara, CA) with a LabView™ code developed by Sahin et al.[19,20] The mechanism of the torsional harmonic technique was based on the higher harmonic vibrations

of a customized T-shaped cantilever, which made it possible to acquire both high frequency vibration and high force to noise ratio.[19,20] In this study, torsional harmonic cantilevers (THC, TL02-300, MikroMasch) of nominal spring constant and resonant frequency of $k = 3$ N m^{-1} and $f_0 = 60$ kHz, respectively, were employed. Elastic modulus E was calculated from the torsional vibration signals based on the Derjaguin–Muller–Toporov (DMT) model,[21] which reduces to the Hertzian spherical elastic contact model for negligible probe–surface adhesion.[22] According to this model, the force–depth response for a spherical probe indenting a flat surface is described by the following equation:

$$F = \frac{4}{3} E^* \sqrt{R}\, d^{3/2} + F_{adh} \qquad (1)$$

where F is the probe–sample interaction force determined directly from cantilever free-end deflection, E^* is the reduced elastic modulus, R is the probe radius (nominally 10 nm for the present cantilevers), d is the indentation depth, and F_{adh} is the force required to† overcome probe–sample adhesion upon unloading.[19,21] Sample elastic modulus E was converted from E^* assuming E and ν of the silicon probe as 165 GPa and 0.23, respectively,[23,24] and $\nu_{sample} = 0.5$. Note that this nanomechanical mapping approach is not currently implemented at elevated temperature, so the mechanical characterization of the bound rubber phase reported here is at room temperature.

Each voxel within these torsional harmonic stiffness maps represents a maximum indentation depth d of 1.5 nm, with a corresponding contact diameter of <10 nm that depends on the local stiffness of the probed material volume. Center-to-center voxel spacing was ~4 nm, representing 256 × 256 indentation responses collected over 1 μm^2 within ~5 min. Thus, approaching the carbon black–polymer interface, one or two indentation contact areas may include both phases. To minimize contributions of the stiff carbon black particles to the inferred elastic properties "near" this interface, in each scan line the two data points on either side of the particle were excluded from analysis of bound rubber elastic moduli. More detailed consideration of potential artifacts of contact-based inference of elastic properties in such nanocomposites is included in the Results and discussion. Note that this torsional, high frequency contact approach provides greater spatial resolution than typical AFM-enabled nanoindentation for two reasons: (1) these torsional cantilevers are sufficiently stiff that load–depth responses can be acquired in compliant materials with high signal–noise ratio at indentation depths ~1 nm and (2) the speed of data acquisition enables collection of these 65 536 load–depth responses without significant thermal drift of the sample (piezostage) over the data acquisition duration. Without the former consideration, greater indentation depths would be required; without the latter consideration, mapping the position and properties of ostensibly fixed nanoscale volumes would not be possible.

2.4.2 Estimation of bound rubber width from harmonic AFM images. Bound rubber content in HNBR–CB ($\Phi_{CB} = 0.05$) was estimated using image analysis, by comparing the average diameter of each CB particle measured from AFM height maps (d_1) and the stiffness maps (d_2). Note here that average diameter is quantified to reflect the non-circular shape of the irregular CB

particles. The average bound rubber width w was then calculated as the difference between apparent diameters in stiffness and height maps for each particle, i:

$$w = (d_{2,i} - d_{1,i})/2 \qquad (2)$$

2.4.3 Numerical simulations to estimate the effect of geometrical confinement on the modulus measurement. To consider how the lateral proximity of the AFM probe to the stiff carbon black particles may affect the inferred bound rubber elastic modulus E_{BR}, we conducted finite element analysis (FEA). These simulations allow systematic consideration of the "edge effect" of indentation near elastically dissimilar interfaces[25–27] and potential effects of geometric confinement. Three-dimensional (3D) FEA simulations were used to estimate this effect on E_{BR}. The model includes indentation *via* a rigid spherical probe at varying distances from a vertical interface between the polymer and carbon black. The simulation mesh is shown in Fig. S1 (ESI†), and contained between 85 407 to 121 933 quadratic (ten-noded) tetrahedral 3D elements for the solid. NLGEOM settings (Abaqus FEA software, Simulia) were used to account for large deformation. Linear elastic behavior of the polymer was assumed; previously FEA has shown that adoption of Mooney–Rivlin or other hyperelastic constitutive models does not significantly alter such indentation finite-scale effects.[28] The indenter was modeled as a discrete rigid body of radius R with 1891 linear quadrilateral elements; traction at the contact interface was not imposed, as adhesion forces in the present experiments did not vary significantly as a function of distance from the carbon black interface. Given the symmetry of this contact, half the indenter and elastic solid were modeled, with a roller boundary condition imposed on the plane of symmetry; the rigid, vertical wall of carbon black was modeled by fixing all degrees of freedom in the orthogonal face. The distance between the probe center and the rigid wall x (*i.e.*, the lateral proximity between the contact point and carbon black interface) was set equal to $0.6R$, R, and $3R$ (6 nm to 30 nm for $R = 10$ nm) to consider the range related to our experiments. Indentation load P and depth h were extracted from a rigid body reference point; maximum indentation depth was set to $0.15R$, in accordance with experiments. The mesh was verified for convergence, and the Hertzian predictions were confirmed for $x \gg R$ (*i.e.*, far from the interface, the assumed input elastic modulus was equivalent to that computed from the output load–depth response).

2.5 Analytical model of composite elastic properties

To analyze the effective Young's elastic modulus of the HNBR–carbon black composite, a prominent micromechanical analytical approach termed the interaction direct derivation (IDD) was employed.[29] This method accounts for inclusion interactions and is widely used for estimation of both elastic properties and conductive properties of composites.[30–32]

The bound rubber shell–carbon black core structure was treated as an effective spherical particle (termed hereafter as an "effective particle") as in Fig. 1a. The corresponding elastic properties were estimated by assuming bound rubber as a matrix
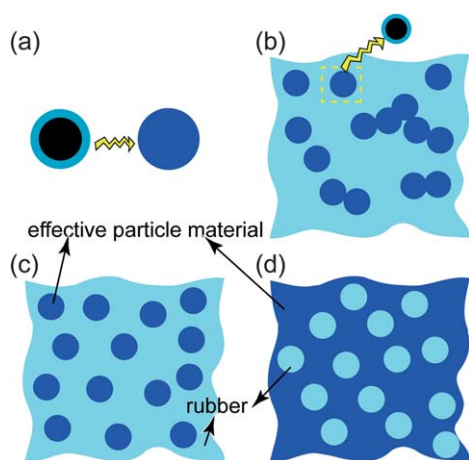
Fig. 1 Schematic of numerical model for particle–polymer nanocomposites exhibiting a mechanical interphase. (a) Carbon black–bound rubber region is equated to an effective particle with equivalent elastic properties. (b) Actual nanocomposites may exhibit partial aggregation among such effective particles. Two extremes of this actual nanocomposite are used to model the mechanical contributions of the bound rubber: (c) effective particles that are well dispersed and isolated within a rubber matrix and (d) full interconnectivity among the effective particles, with isolated regions of the rubber matrix.

surrounding a carbon black particle.[33] Since the bound rubber shell and carbon black core are both assumed elastically isotropic, the effective spherical particle is also elastically isotropic. With the IDD estimate method, we obtain the compliance tensor of the effective particles (S_{ijkl}), from which any two independent elastic constants of the isotropic description can be obtained. Calculation of the effective Young's elastic modulus E_p and Poisson's ratio v_p of the effective particles is expressed most concisely as a system of equations:

be obtained *via* eqn (3). The parameters of bound rubber and carbon black are replaced with those of bulk rubber and effective particles, respectively. Note that here the volume fraction of effective particles is then represented as $\Phi_p = \Phi_{CB}/a$ instead of a. However, the non-contacting assumption is violated in the actual carbon black–rubber composites due to particle agglomeration.[1,3,5,8] In an actual nanocomposite (Fig. 1b), contact between CB particles obfuscates clear delineation between a matrix phase and an inclusion phase. For such complex composite morphologies, the self-consistent method (SCM)[34] is applicable and widely used. However, the solutions of such an approach are implicit and require assumed values of interphase thickness and elastic properties. Thus, such a method is not appropriate for the current study, in which we seek to infer interphase properties that are consistent with both our nanoscale characterization of the phase thickness and stiffness and macroscale characterization of the composite elastic modulus.

The actual nanocomposite is thus treated in the following manner. The morphology of the actual nanocomposite (Fig. 1b) is regarded between two extreme cases: non-contacting effective particles (Fig. 1c) and fully interconnected effective particles (Fig. 1d). In the interconnected case, effective particles formed a connected domain, while the rubber phase exists as several isolated regions. Thus, the effective particle phase is treated as the matrix, and the bulk rubber phase is treated as an inclusion phase (with a shape designated as spheres such as voids in a granular material).[35] For the interconnected case, the elastic properties (E_{cont} and v_{cont}) were obtained in eqn (3) by replacing E_{BR} and v_{BR} with E_p and v_p, and E_{CB} and v_{CB} with E_r and v_r.

Elastic properties (compliance tensor S_{ijkl} or stiffness tensor C_{ijkl}) of the actual nanocomposite are adopted as a linear superposition of these two cases, weighted by the volume fraction of each matrix phase ($1 - \Phi_p$ for non-contacting inclusions and Φ_p for interconnected inclusions). Thus, the effective elastic

$$\frac{E_{BR}}{E_p} = \left((1 - 2v_{BR}) + \frac{3\big((1 - 2v_{CB})E_{BR}/E_{CB} - (1 - 2v_{BR})\big)a}{3 + 2(1 - a)\big((1 - 2v_{CB})E_{BR}/E_{CB} - (1 - 2v_{BR})\big)\big/(1 - v_{BR})} \right) \frac{1}{(1 - 2v_p)}$$

$$\frac{E_{BR}}{E_p} = \left((1 + v_{BR}) + \frac{15\big((1 + v_{CB})E_{BR}/E_{CB} - (1 + v_{BR})\big)a}{15 + 2(1 - a)\big((1 + v_{CB})E_{BR}/E_{CB} - (1 + v_{BR})\big)(7 - 5v_{BR})/(1 - v_{BR}^2)} \right) \frac{1}{(1 + v_p)}$$

(3)

where subscripts BR and CB indicate the elastic properties of bound rubber and carbon black, respectively, that comprise the effective particle, and Φ_{BR} and Φ_{CB} are the volume fraction of carbon black and bound rubber, respectively. Here, a is the volume fraction of carbon black in the effective particles, such that $a = \Phi_{CB}/(\Phi_{BR} + \Phi_{CB}) = [r/(w + r)]^3$, where r is the average radius of the carbon black particle and w is the average bound rubber width. Next, the effective elastic properties of the entire composite were estimated by repeating this procedure, wherein the effective particle (carbon black surrounded by bound rubber) is surrounded by the bulk rubber matrix. If the high degree of dispersion is achieved and effective particles are isolated, the IDD model applies so that the elastic properties for a nanocomposite comprising non-contacting particles (E_{nc} and v_{nc}) can

constants E_{comp} and v_{comp} of the overall nanocomposite are obtained as follows:

$$\frac{E_{comp}}{(1 - 2v_{comp})} = \left(1 - \Phi_p\right) \frac{E_{nc}}{(1 - 2v_{nc})} + \Phi_p \frac{E_{net}}{(1 - 2v_{net})}$$

$$\frac{E_{comp}}{(1 + v_{comp})} = \left(1 - \Phi_p\right) \frac{E_{nc}}{(1 + v_{nc})} + \Phi_p \frac{E_{net}}{(1 + v_{net})}$$

(4)

This approach has the result that when Φ_p is very small, effective particles tend to be dispersed discretely, and that when Φ_{CB} increases, local particle contact and formation of at least isolated networks across the material will occur; this trend is physically plausible.

Elastic properties of carbon black powders are not well defined experimentally, and thus the properties of graphite were assumed
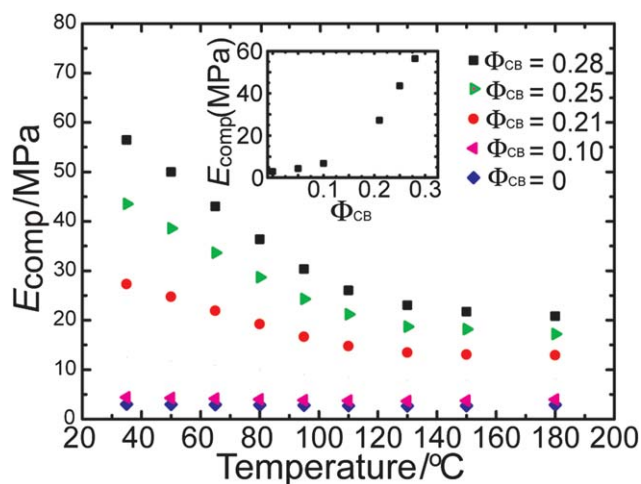
Fig. 2 Macroscale elastic modulus as a function of temperature for pure HNBR and HNBR–carbon black (Φ_{CB} = 0.05–0.28), measured using DMA. Inset: elastic modulus of HNBR and the composites as a function of Φ_{CB} at a fixed temperature of 35 °C.

(E_{CB} = 10 GPa, v_{CB} = 0.3). Elastic moduli of HNBR were taken from our AFM-enabled indentation experiment (E_{HNBR} = 4 MPa) and Poisson's ratios of the bound rubber and rubber were both assumed as 0.499. Finally, the radius of carbon black particles was chosen as the average radius of carbon black (including carbon black aggregates) measured from AFM height images such as shown in Fig. 5, which was 56 nm.

3 Results and discussion

3.1 Macroscale analysis: observations supporting existence of bound rubber

Fig. 2 shows elastic moduli of pure HNBR and HNBR–CB nanocomposites (Φ_{CB} = 0.05 to 0.28) as measured *via* dynamic mechanical analysis (DMA), adapted from ref. 9. Several important observations of this macroscale analysis are noted here. First, the measured elastic modulus E of pure HNBR was essentially invariant with temperature (3 MPa at 35 °C). Second, Fig. 2 (inset) illustrates that E of HNBR–CB composites increased non-linearly with increasing vol% carbon black, such that E increases approximately 13-fold for a Φ_{CB} increase from 0.05 to 0.28. This non-linear dependence on filler content may be explained by one of two possible scenarios, or both. In the first scenario, the volume percentage of bound rubber, which is assumed stiffer than the elastomeric matrix, increased dramatically as more filler particles were added to the rubber matrix. In the second scenario, the number of particle agglomerates was increased at higher Φ_{CB}, thus favoring formation of a continuous carbon black phase that can bear higher stress.

Finally, a marked decrease of storage modulus with increasing temperature was observed for all composite samples (*e.g.*, from 56.4 to 20.8 MPa for HNBR–28 vol% CB at 180 °C). Robisson originally proposed that such a temperature-dependent stiffness was due to a concurrent decrease in bound rubber width/thickness around filler particles with increasing temperature.[9] In other words, it was hypothesized that the volume fraction of stiff interphase between the rubber matrix and filler particles was
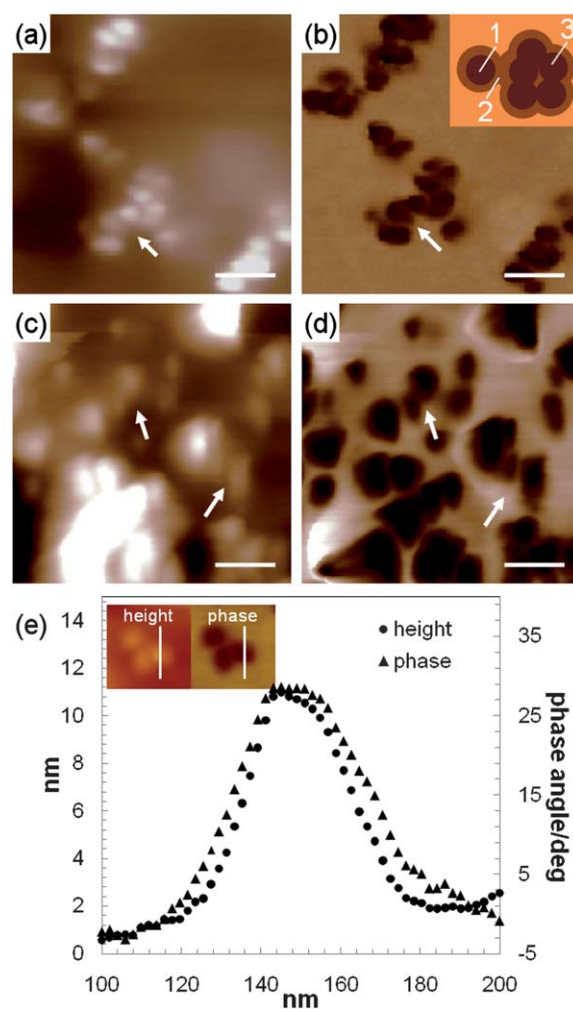

Fig. 3 Atomic force microscopy (AFM) height and phase images, respectively, for (a, b) HNBR–5 vol% CB and (c, d) HNBR–28 vol% CB. Inset schematic of (b) indicates (1) CB particles surrounded by (2) bound rubber, as well as (3) particle aggregates. (e) Height and phase profiles on the same particle cluster (AFM height and phase, inset). Arrows indicate the particle aggregates and the "connecting filaments" in aggregates. Scale bars = 100 nm.

reduced at high temperature. We note that this phenomenon was also observed for uncrosslinked versions of these materials: significant dissolution of the rubber phase in acetone occurred only for uncrosslinked HNBR–5 vol% CB, and not for uncrosslinked HNBR–28 vol% CB, suggesting a major volume fraction of dissolution-resistant bound rubber for high Φ_{CB}.[9,16] Considering these observations, we next sought to visualize and characterize the properties of such a bound rubber within the crosslinked composites.

3.2 Phase morphology of HNBR/CB composites

Fig. 3 shows topography and phase-lag images of HNBR–5 vol% CB and HNBR–28 vol% CB samples, acquired at room temperature *via* tapping mode AFM (Fig. 3a and c, height images, Fig. 3b and d, phase images.) These images relate several key points. First, in comparing the height and phase images for each CB particle (specifically, the actual line scans that comprise

these image projections), the phase profile was consistently wider than the corresponding height profile (Fig. 3e). If one treats the CB particle regions as spheres, the effective radius of the phase profile is 6–10 nm wider than that measured from the height profile of the same CB particle region. This suggests the existence of a mechanically distinct layer around CB particles, of thickness ~10 nm. We take this layer of distinct phase lag to represent the bound rubber phase. (We will discuss quantification of this layer thickness and stiffness via more detailed approaches in Sections 3.4 and 3.5.)

Second, Fig. 3 shows that particle agglomeration (arrows) occurred at both low and high Φ_{CB}, although many fewer agglomerates exist in the lower CB-content composite. Phase images indicate that bound rubber forms are not only around the perimeter of such particle aggregates but also in between particles or aggregates (also termed "connecting filament",[5] indicated by arrows in Fig. 3). This phenomenon is demonstrated schematically in the inset of Fig. 3b, illustrating that the existence and properties of all bound rubber phases within such a composite should be considered. To visualize and characterize the elastic properties of this bound rubber via nanomechanical contact, we next focused on the HNBR–5 vol% CB as a model composite, in which we can assume minimal particle agglomerations or connecting filament bound rubber content.

3.3 AFM visualization of bound rubber content at elevated temperature

To consider whether the apparent bound rubber content decreased with increasing temperature, as had been inferred from the above macroscale mechanical experiments, HNBR–5 vol% CB was imaged via AFM with an integrated in situ heating stage. Fig. 4 shows both the height and phase images obtained on the same sample area at room temperature (Fig. 4a–c) and at 180 °C

(Fig. 4d–f). As the temperature increased from room temperature (~25 °C) to 180 °C, no obvious morphological changes were observed in height images, demonstrating that the position and number of CB aggregates was invariant with temperature. In contrast, phase images obtained over the same group of particles showed a significant contrast difference as a function of increasing temperature. At 180 °C, the apparent particle diameter indicated by phase images decreased and the edges around these particles became sharper, as consistent with decreased bound rubber content surrounding these particles at elevated temperature. Further analysis of the image linescans was conducted to quantify this change in bound rubber content via the apparent diameter of CB–bound rubber particles in phase images. Apparent average radius r_c is the sum of both the CB particle radius r_p and the surrounding bound rubber w. At room temperature, r_c was 56 ± 20 nm, and decreased for the same group of particles to 45 ± 19 nm at 180 °C. This indicates a change in bound rubber width w of ~11 nm.

Certainly, at higher temperatures, the chain mobility within the "connecting filament" bound rubber between particles or particle aggregates is also increased. Thus, the elastic modulus of connecting filaments decreases toward that of the rubber matrix, effectively reducing the degree of particle agglomeration. This reduced agglomeration of bound rubber-encapsulated particles could also give rise to a decrease in macroscopic elastic properties. Again, here we chose to study a composite of a low carbon black content ($\Phi_{CB} = 0.05$) to minimize the number of agglomerates and thus the contribution of connecting filaments.

3.4 Estimation of bound rubber width and elastic modulus via torsional harmonic AFM

Although AFM phase lag images indicate the potential for a mechanically distinct interphase about the carbon black, with
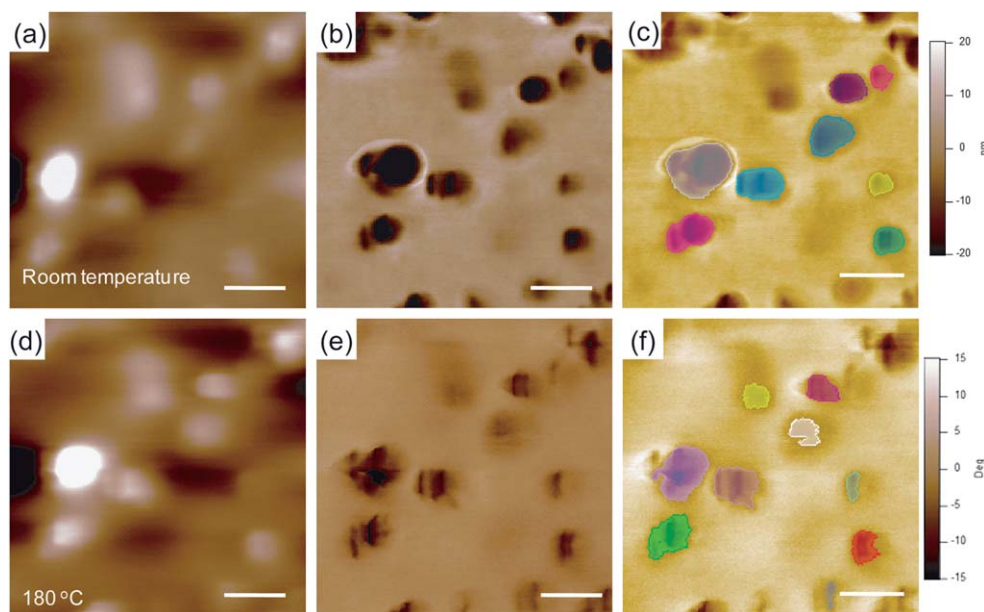

Fig. 4 AFM (a) height and (b) phase lag images of HNBR–5 vol% CB at room temperature (RT). (c) Image analysis of height image at RT. (d) Height and (e) phase images of the same particles acquired at 180 °C. (f) Analysis of the phase images showed that the particle diameters decreased approximately 11 nm as the temperature increased from RT to 180 °C. Scale bars = 200 nm.

darker pixels suggestive of increased energy dissipation, the elastic properties of pixels within such images are difficult to interpret quantitatively. Indeed, the phase lag in such images is due to energy dissipation arising from both viscoelastic deformation and adhesion to the probe. To further understand the mechanical property variation within these composites, especially the elastic properties of the bound rubber, additional experiments were conducted using torsional harmonic AFM. This approach enables determination of stiffness at each image voxel, in terms of elastic modulus determined from the DMT adhesion model (see Materials and methods). Potential artifacts of indenting in close proximity to CB particles were considered quantitatively.

3.4.1 Nanomechanical estimate of bound rubber width.

Fig. 5a and c indicate the height and stiffness maps, respectively, for HNBR–5 vol% CB over a surface region of 1 μm². Stiffness maps indicate elastic modulus at each voxel according to eqn (1); representative load–depth responses are shown in Fig. 10a. Note that the stiffness profiles across the CB particles are wider than those of height profiles, with the stiffness in these regions surrounding the particles exceeding that of the rubber matrix by approximately one order of magnitude. Idealizing the particle aggregates as spheres, the average CB particle radii as measured from height and stiffness maps were 56 ± 24 nm and 75 ± 26 nm, respectively. Thus, an average bound rubber width $w = 19 \pm 8$ nm was obtained from this direct image analysis (Fig. 5b and d). Given the voxel spacing and exclusion of points nearest this CB interface due to potential probe shape convolution and contact area overlap in these maps (see Materials and methods), this
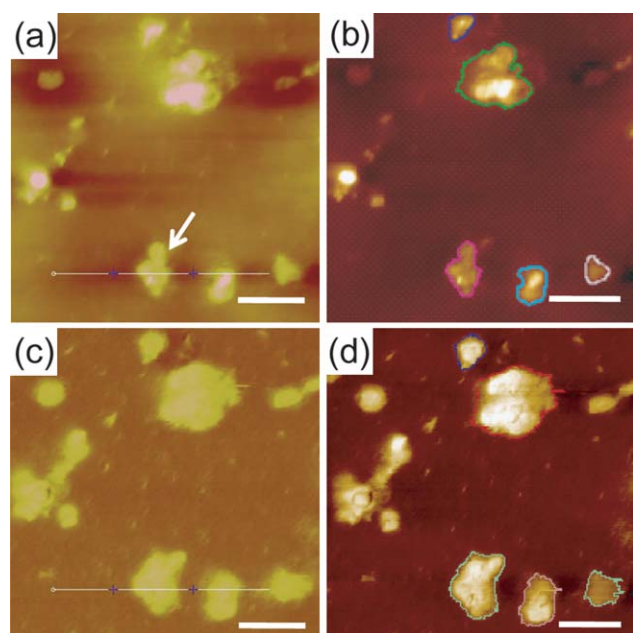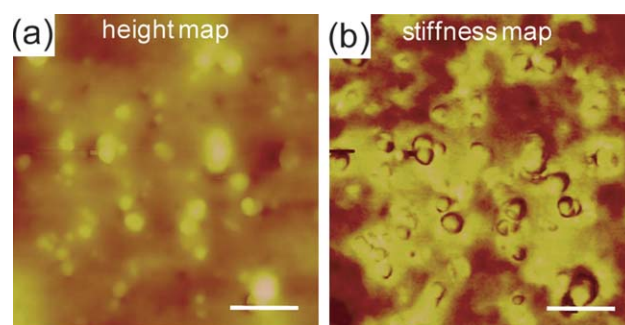

Fig. 6 Torsional harmonic AFM (a) height and (b) stiffness maps of HNBR–28% carbon black. Stiffness maps show approximately 67% of the sample surface (bright regions) exhibits elastic moduli exceeding that of the HNBR matrix. Scale bars = 200 nm.

bound rubber width exceeds the uncertainty zone extending as much as ~8 nm from the CB interface.

Assuming that this bound rubber width w and average CB particle radius $r = 56$ nm will not change with increasing carbon black content, we can then estimate the vol% of this stiff phase expected in the composite of higher vol% CB ($\Phi_{CB} = 0.28$). This stiff region is defined by the volume fraction ($\Phi_P = \Phi_{BR} + \Phi_{CB} = \Phi_{CB} [(w + r)/r]^3$). Using these experimentally determined averages of $r = 56$ nm and $w = 19$ nm, this stiffer volume fraction ($\Phi_{BR} + \Phi_{CB}$) is 0.67 for a carbon black concentration of $\Phi_{CB} = 0.28$. Indeed, this calculated estimate agrees well with the harmonic AFM experimental observation for HNBR–28 vol% CB in Fig. 6, in which the measured volume fraction of the stiff (bright) phase from images such as Fig. 6b is ~70%.

Fig. 5 Torsional harmonic AFM (a) height and (c) stiffness maps of HNBR–5% carbon black composite. Arrow indicates one carbon black particle cluster. (b and d) Image analysis of CB particle perimeters (colored traces) in both height and stiffness maps indicates that the apparent CB particle diameter is ~38 nm larger than that measured from height maps. Scale bars = 200 nm.
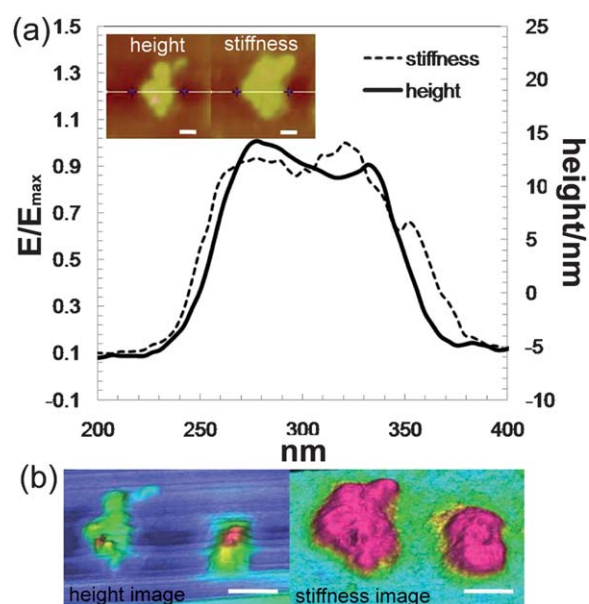

Fig. 7 (a) Comparison of particle profiles measured on torsional harmonic AFM height and stiffness maps of the same particle cluster. Stiffness profile diameters exceed height profiles by ~30 to 40 nm. Scale bar = 50 nm. (b) Three-dimensional rendering of height and stiffness images. Scale bar = 100 nm.

3.4.2 Nanomechanical estimate of bound rubber elastic modulus.

Fig. 7 shows an example of the height and normalized elastic modulus E/E_{max} profile across one CB particle (AFM image, inset), where $E_{max} = 1390$ MPa. In all such linescans of these stiffness maps, the projected contact area and spacing of torsional harmonic indentations enabled collection of responses spaced by ~4 nm to depths of 1.5 nm and contact diameters of ~10 nm (i.e., voxels in stiffness maps). From geometric considerations, the two indentation responses nearest either side of the carbon black aggregates in each linescan could comprise geometric overlap between the probe and CB profiles, or could comprise projected contact areas including both the carbon black and the polymer regions, and these voxels were thus excluded from calculation of elastic moduli (see Materials and methods). These data show clearly that the apparent stiffness of bound rubber is approximately one order of magnitude higher than that of the rubber matrix for these HNBR–carbon black composites. Using the height map as a reference, we averaged the elastic modulus obtained from the stiffness map for E_{BR} and E_{HNBR}. However, comparing to the macroscale mechanical analysis of HNBR ($E_{HNBR} = 3$ MPa), the stiffness obtained via this nano-indentation on this rubber matrix is much higher (170 ± 39 MPa). Sahin and Erina have also noted that elastic moduli of elastomeric blocks in block copolymers measured via this technique exceeded literature values of bulk forms of this phase.[19] They reasoned that either the high loading frequency of this measurement or the geometrical confinement of the stiffer phase could account for the apparent stiffening of the elastomeric block. However, in the present study, even on the HNBR matrix that is far away from any CB particles, we measured a high elastic modulus as compared to our own DMA macroscale analysis of HNBR (Fig. 5c). Thus, we believe that this difference in magnitude is due to the difference in loading frequencies between the macroscale and nanoscale approaches used to analyze this viscoelastic nanocomposite, as summarized here.

As a polymer, HNBR exhibits both time- (frequency) and temperature-dependent properties during deformation. Torsional harmonic AFM-enabled indentation requires a high-frequency T-shaped cantilever to probe the elastic properties of materials near the resonance frequency of these cantilevers (10 s kHz).[19,20] This high frequency can result in a higher apparent stiffness of elastomers than that measured using typical low-frequency macroscale mechanical testing such as DMA (~1 Hz). We thus accounted for the time-dependent behavior based on the macroscale elastic properties obtained using the well known Williams–Landel–Ferry (WLF) theory.[18,36] This temperature-frequency equivalence approach, detailed in the ESI†, enabled us to relate the measured elastic moduli of the bound rubber (measured via torsional harmonic AFM-enabled indentation) to that anticipated in lower-frequency DMA experiments. Construction of an experimental master curve for the HNBR matrix (Fig. 8a) was used to determine a shift factor of 4.7. We applied this WLF shift to the AFM-measured elastic moduli of bound rubber, defined as points within 20 nm of the carbon black perimeter. We predict that at room temperature and a loading frequency of 1 Hz, the bound rubber stiffness will be $E_{BR} = 53 \pm 11$ MPa (mean ± standard deviation). Thus, under these conditions the bound rubber exists in a mechanical transition between the glassy and the rubbery states.
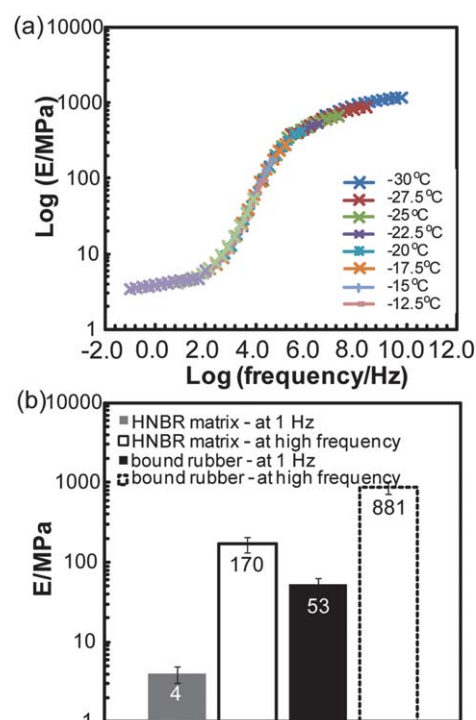

Fig. 8 (a) Master curve of HNBR elastic modulus at different temperatures and frequencies; (b) comparison of elastic modulus obtained at the resonance frequency of the torsional harmonic AFM cantilever and at low frequency consistent with macroscale mechanical experiments.

Fig. 8b shows the measured values of elastic moduli for HNBR and bound rubber via torsional harmonic AFM, as well as the magnitudes predicted at 1 Hz according to this master curve. The frequency-shifted elastic moduli of the HNBR matrix and bound rubber are 4 ± 1 MPa and 53 ± 11 MPa, respectively. Note that the average elastic moduli of the HNBR matrix as determined from macroscale DMA and torsional harmonic AFM agree within 1 MPa when scaled appropriately. Such considerations of time-dependent effects on inferred elastic properties are required to compare experiments on elastomers/polymers obtained via macroscale, low-frequency experiments with those obtained AFM-enabled indentation with a high resonance frequency cantilever.

3.4.3 Consideration of finite thickness and geometric confinement effects on contact-based analysis of nanocomposites.

Accurate determination of elastic properties of nanocomposites via contact-based imaging and mechanical deformation requires careful consideration of the finite dimensions of the nanoscale phases and the mechanical probes used to deform the material near those phases.[37,38] Here, we consider two different potential artifacts that would cause the region near particle–rubber interface to appear stiffer, and thus would negate the hypothesis: indenting a thin rubber phase located above a stiffer carbon-black substrate and indenting a rubber phase located adjacent to a stiffer carbon-black region.

First, it is reasonable to consider whether the increased stiffness of the bound rubber region is an artifact of indenting this film of finite thickness that might sit atop underlying CB
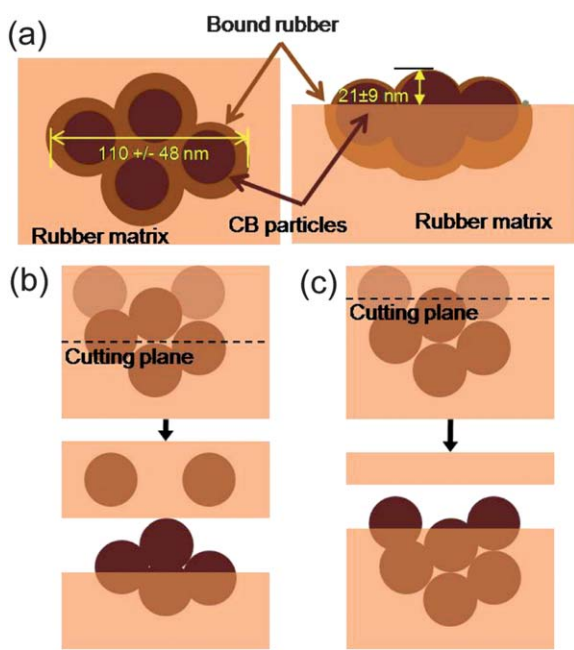
Fig. 9 (a) Schematic of carbon black particle cluster size and height. Left: plan view after cryotoming. Right: side view after cryotoming. (b) Cryotoming knife may cut a plane through a particle cluster or (c) may simply expose the surface of an intact particle cluster.

particles. When indenting a film atop a stiff, hard substrate, it is true that the measured elastic modulus of the film can exceed the actual value due to the mechanical contributions of loading resistance from the underlying substrate.[39] For the present case, however, quantitative image analysis of the particle topography indicates that it is unlikely that the CB particle lies beneath the indentation plane of the bound rubber regions. Specifically for these cryotomed samples, we find through AFM height images that the average CB particle radius is 56 ± 24 nm, whereas the average cluster height is 21 ± 9 nm. This cluster height is quite comparable to the average particle diameter of N330 CB (26–30 nm (ref. 17)). Such topography indicates that although there is significant variation in cluster in-plane diameter, after cryotoming, the CB particles at the surface are exposed to half (or more) of the particle diameter (Fig. 9a). This may result from the cryotome knife cutting through particle aggregates to remove some particles (Fig. 9b) or along the surface of an intact aggregate (Fig. 9c). It remains possible that a small amount of bound rubber remained adhered to the CB particle surfaces after cryotoming, but for the purpose of our calculations we assumed here that most of the bound rubber was removed from particle surface *via* cryotoming. As the CB regions extend from the exposed surface to typically more than half the CB nanoparticle diameter, this suggests that there are no nanoparticles tightly packed beneath the exposed surface at the cluster perimeter. Thus, one can reasonably assume that there is no stiff, hard region just below the surface of the exposed CB particle perimeter. The elastic properties measured for this region would then not be strongly affected by "substrate effects". This assumption is further supported by the consideration of paired height and stiffness maps such as Fig. 5, where the CB particles are always wider in stiffness maps as compared to height maps. If the relative widening of features in the stiffness maps was due to the

presence of underlying carbon nanoparticles, this would imply that all CB particles were always cryotomed to less than half the cluster diameter, which is statistically highly unlikely.

Second, it is possible that indentation of a compliant material that is immediately adjacent to a stiffer material (*i.e.*, indenting near the edge or interface between the two) will cause an artificial increase in apparent elastic modulus of the more compliant phase. Semi-analytical models of this edge-proximity effect have been proposed recently,[25,26] but relate the plastic zone dimensions to this interface distance *via* material hardness; that approach does not apply to the elastomers considered here. For the present case, we conducted finite element simulations to estimate the effect of measured E as a function of distance between the contact point and a rigid sidewall representing the carbon black. In these simulations, the bound rubber was not modeled explicitly as a separate phase; rather, indentation responses were extracted from normal Hertzian contact points at varying distances between the HNBR phase and a rigid CB sidewall (see Methods). Fig. 10a shows representative experimental load–depth responses acquired on the HNBR matrix far from this interface, on the bound rubber region near this interface, and on CB particles. These responses differed visually and quantitatively as a function of position with respect to the CB interface; adhesion forces identified *via* this high-frequency method[19,20] did not vary significantly between the HNBR and bound rubber regions ($\sim$2 nN). Note that the maximum displacement in these experimental responses was $\sim$1.5 nm for probe radius $R \approx 10$ nm. Fig. 10b and c show the simulated minimum principal stress contours and load–depth responses, scaled for the same indentation depth and range of lateral distances x from the CB interface ($0.6R < x < 3R$). Fig. 10b shows that when $x \leq R$, the stress contours are distorted by the presence of the rigid interface, and Fig. 10c shows that this distortion is manifested by increased curvature in the simulated load–depth response. Fig. 10d shows the effect of this proximity on the magnitude of E computed from the simulated load–depth response in terms of E_x/E_{inf}, where E_x is the computed elastic modulus at $0.6R < x < 3R$ and E_{inf} is the elastic modulus infinitely far from the rigid CB interface. The magnitude of E_{inf} agreed with the assumed elastic modulus of the simulated constitutive model within 4%, serving as a baseline error for extracting the elastic properties from the simulated indentation response. This figure makes clear that the magnitude of E_{BR} extracted from the indentation response increases by 40% for lateral distance $x = 0.6R$ (or 6 nm away) and by only 15% for $x = R$ (or 10 nm away). In contrast, the present experiments show that the measured E_{BR} (53 ± 11 MPa), reported as an average over the region extending from $\sim$6 nm $< x$ $<\sim$20 nm from the CB interface, exceeds that of the HNBR matrix (4 MPa) by more than an order of magnitude. Indeed, indentations closer to this interface than $x \approx 6$ nm were intentionally excluded from our analysis of bound rubber stiffness to minimize such lateral proximity contributions and probe shape convolution. Thus, we conclude that proximity to underlying stiff substrates and adjacent stiff sidewalls can indeed contribute systematic error to interpretation of such experiments, and should be considered carefully in such nanomechanical analysis of nanocomposites. However, having quantified these effects, we find that the significant stiffening of the bound rubber regions that we observe here cannot be attributed chiefly to such effects.
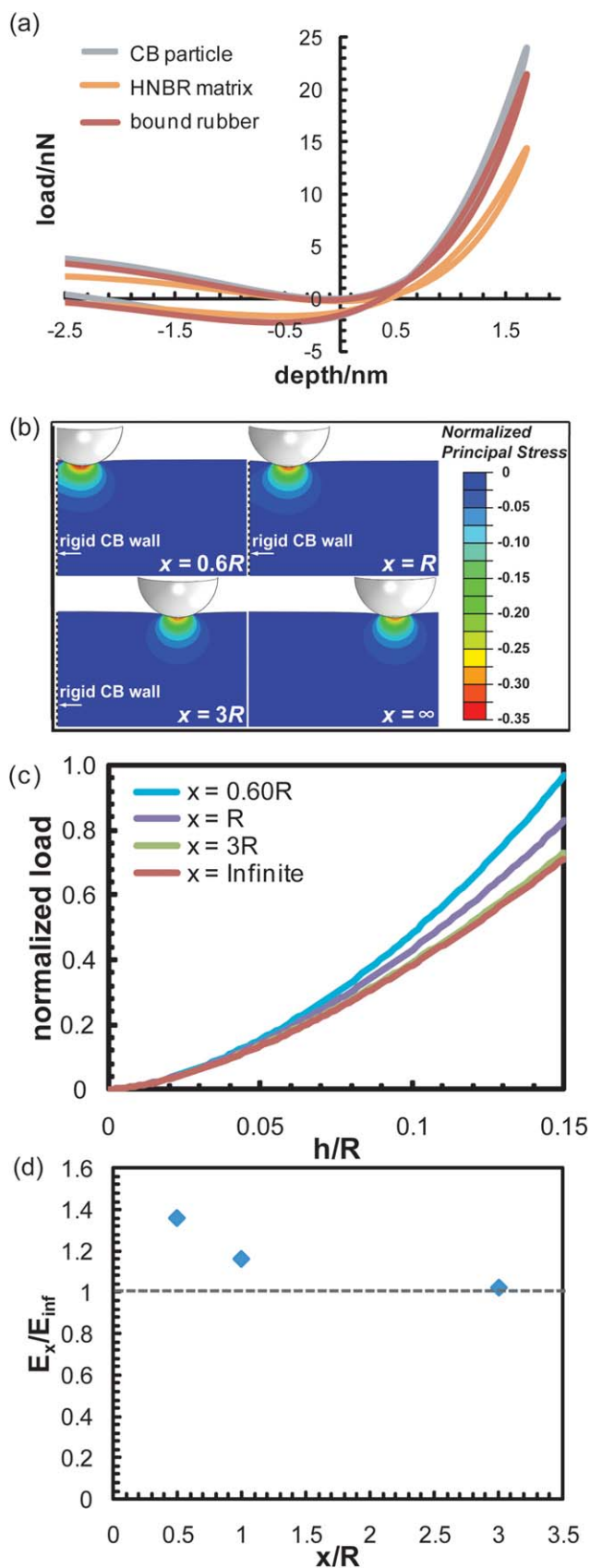
Fig. 10 (a) Experimental load–depth responses on HNBR far from the CB particles, on the bound rubber region, and on CB particles. (b) Finite element simulations as a function of distance from the rigid CB interface

3.5 Theoretical predictions of bound rubber elastic modulus and width

The micromechanical model described by eqn (3) and (4) was used to predict the elastic modulus E_{BR} and width w of the bound rubber phase. These equations were first solved to identify the values of E_{BR} and w that would correlate most strongly (*i.e.*, 0.97 $< R^2 < 1$) with E_{comp} over the entire range of vol% carbon black at the lowest temperature considered in Fig. 2 (35 °C). Thus, the parameter pairs are reported as a range over this R^2 optimization criterion, where E_{BR} is 30–58 MPa and the corresponding interphase width w is 27–14 nm. This range agrees well with that measured at room temperature *via* torsional harmonic AFM imaging and mechanical analysis (E_{BR} = 53 ± 11 MPa and w = 19 ± 8 nm).

To extend this prediction to the range of sample temperatures considered in macroscopic E_{comp} of Fig. 2, we then assumed E_{BR} constant and w to decrease with increasing temperature according to an Arrhenius relation:

$$\Phi_{BR} = \Phi_{CB}b \exp\left(\frac{E_{adsorb}}{RT}\right) \quad (5)$$

where E_{adsorb} is the adsorption energy of carbon black to rubber,[11,40,41] b is a dimensionless factor and R is the gas constant 8.31 J k^{-1} mol^{-1}. At sufficiently high vol% CB, it is also possible that increasing temperature results in decreasing aggregation of the bound rubber that serves as a connecting filament. Thus, the stiffness tensor of this connecting filament network is also proportional to the volume fraction of bound rubber Φ_{BR}, modifying eqn (4) with eqn (5) to obtain:

$$\frac{E_{comp}}{(1 - 2v_{comp})} = (1 - \Phi_p)\frac{E_{nc}}{(1 - 2v_{nc})}$$
$$+ \Phi_p \exp\left(\frac{E_{adsorb}}{R}\left(\frac{1}{T} - \frac{1}{308}\right)\right)\frac{E_{net}}{(1 - 2v_{net})}$$
$$\frac{E_{comp}}{(1 + v_{comp})} = (1 - \Phi_p)\frac{E_{nc}}{(1 + v_{nc})}$$
$$+ \Phi_p \exp\left(\frac{E_{adsorb}}{R}\left(\frac{1}{T} - \frac{1}{308}\right)\right)\frac{E_{net}}{(1 + v_{net})} \quad (6)$$

From eqn (3), (4), (6) and experimentally measured Young's elastic modulus of the HNBR–28 vol% CB composite as a function of temperature (35 °C to 180 °C in Fig. 2), we obtained E_{BR}, b and E_{adsorb} as 48 MPa, 0.09 and 7.063 kJ mol^{-1}, respectively. Note that Young's modulus of the bound rubber calculated across this wide range of temperatures is within the range of fitted E_{BR} calculated above at 35 °C, for composites with a range of vol% CB. This supports our assumption that E_{BR} does not depend strongly on temperature over this range. Further, the calculated magnitude of E_{adsorb} agrees well with that reported by Dessewffy.[41] Using these fitted values obtained at Φ_{CB} = 0.28, we can then predict E_{comp} as a function of temperature for all other volume fractions of carbon black. Fig. 11 shows the success of

x at *x* = 0.6*R*, *R*, 3*R* and infinity show distortion of the minimum principal stress at *x*. The rigid CB walls are on the left side of each contour. (c) Simulated load–depth responses at *x* = 0.6*R*, *R*, 3*R* and infinite. (d) E_x/E_{inf} at different *x/R*, E_x is the simulated modulus and E_{inf} is the elastic modulus calculated at *x* ≫ *R*.
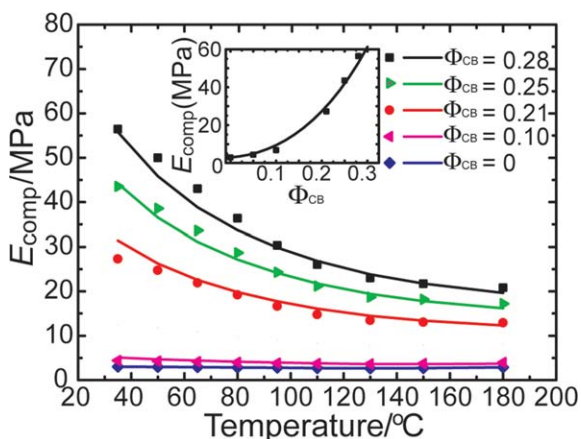
Fig. 11 Comparison of experimental data (points) and numerical results (lines) based on analytical IDD model discussed in the text, for Young's modulus of HNBR–carbon black composites as a function of temperature. Inset: comparison of the experimental (points) and numerical (line) results at different Φ_{CB} for a fixed temperature of 35 °C.
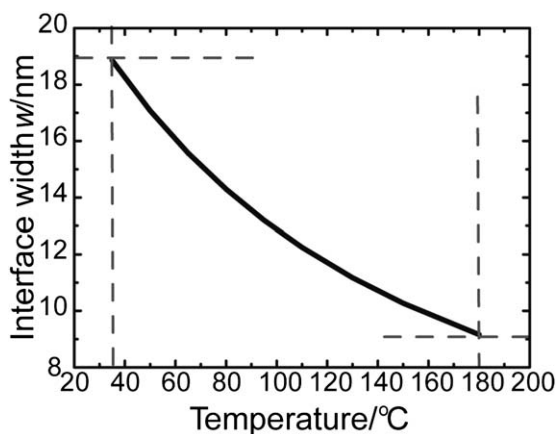

Fig. 12 Predicted relation between interphase width and temperature for HNBR–CB composite, according to the analytical IDD model discussed in the text. The predicted decrease in interphase width agrees well with that measured experimentally *via in situ* AFM imaging of the nanocomposite over the same temperature range.

this numerical prediction as a function of temperature, which assumes only that the bound rubber width decreases with temperature according to eqn (4). Importantly, this three-phase model also captures the non-linear increase in E_{comp} with increasing Φ_{CB} (Fig. 11, inset).

This theoretical model also allows us to predict the change in bound rubber width with temperature. As in the experiments, we assume that the effective particles are approximately spherical, and determine from our model $a = \Phi_{CB}/(\Phi_{BR+} + \Phi_{CB}) = [r/(w + r)]^3$. Fig. 12 shows this calculated change in width with temperature, predicting $w = 18.9$ nm at 35 °C. This agrees well with our torsional harmonic AFM measurements at 35 °C ($w = 19 \pm 8$ nm, see Fig. 5). Fig. 12 also shows that the predicted decrease in bound rubber width for an increase in temperature from 35 °C to 180 °C is approximately 10 nm. This change in predicted bound rubber width is in good agreement with the experimentally measured change in w over this same temperature range (11 nm, see Fig. 4).

4 Conclusions

In this study, we demonstrated novel methods to visualize and to characterize the properties of bound rubber, a generally accepted polymer phase that extends between the particle and elastomer interface. Uniaxial tension of HNBR–CB composites indicated decreasing elastic moduli with temperature, and a non-linear increase in elastic moduli with increasing vol% CB. *In situ* annealing and AFM imaging of these composites showed directly that the bound rubber content decreased with temperature, in quantitative agreement with our numerical model of the composite. The elastic modulus and width of this bound rubber were measured *via* torsional harmonic AFM indentation at room temperature, and several potential challenges and misinterpretations from such experiments were considered. Both the elastic moduli and width of the stiffer bound rubber region agreed well with our numerical model of the nanocomposite's elastic properties. Together, these results provide the first direct observation and validation of bound rubber as a mechanically distinct, nanoscale phase that strongly modulates the elastic properties of elastomer–carbon black nanocomposites. We anticipate that such approaches can enable future studies which seek to modify the extent of interaction between carbon-based fillers and elastomers, in terms of both interphase properties and macroscopic performance.

Acknowledgements

References

1 J. B. Donnet, *Compos. Sci. Technol.*, 2003, **63**, 1085–1088.
2 A. Voet, *J. Polym. Sci., Macromol. Rev.*, 1980, **15**, 327–373.
3 J. Berriot, F. Martin, H. Montes, L. Monnerie and P. Sotta, *Polymer*, 2003, **44**, 1437–1447.
4 D. Goritz, H. Raab, J. Frohlich and P. G. Maier, *Rubber Chem. Technol.*, 1999, **72**, 929–945.
5 J. L. Leblanc, *Prog. Polym. Sci.*, 2002, **27**, 627–687.
6 V. M. Litvinov and P. A. Steeman, *Macromolecules*, 1999, **32**, 8476–8490.
7 A. C. Patel and J. T. Byers, *Rubber India*, 1982, **34**, 9–13.
8 A. C. Patel and K. Lee, *Elastomerics*, 1990, **122**, 14–18.
9 A. Robisson, *Mech. Mater.*, 2010, **42**, 974–980.
10 M.-J. Wang, *Rubber Chem. Technol.*, 1998, **71**, 520–589.
11 S. Wolff, M.-J. Wang and E.-H. Tan, *Rubber Chem. Technol.*, 1993, **66**, 163–177.
12 P. B. Stickney and R. D. Falb, *Rubber Chem. Technol.*, 1964, **37**, 1299–1340.
13 G. Simon, K. Baumann and W. Gronski, *Macromolecules*, 1992, **25**, 3624–3628.
14 J. Rault, J. Marchal, P. Judeinstein and P. A. Albouy, *Eur. Phys. J. E: Soft Matter Biol. Phys.*, 2006, **21**, 243–261.
15 N. Kida, M. Ito, F. Yatsuyanagi and H. Kaido, *J. Appl. Polym. Sci.*, 1996, **61**, 1345–1350.
16 A. Robisson and B. Chartier, *Role of the Interphase on Reinforcement of Filled Rubbers: Influence of Temperature, Carbon Black Content and Strain*, Taylor & Francis Group, London, 2010.
17 ASTM Standard, Philadelphia, 1996.

18 M. L. Williams, R. F. Landel and J. D. Ferry, *J. Am. Chem. Soc.*, 1955, **77**, 3701–3707.
19 O. Sahin and N. Erina, *Nanotechnology*, 2008, **19**, 445717.
20 O. Sahin, S. Magonov, C. Su, C. F. Quate and O. Solgaard, *Nat. Nanotechnol.*, 2007, **2**, 501–514.
21 J. N. Israelachvili, *Intermolecular and Surface Forces*, Academic Press, London, 1992.
22 K. L. Johnson, *Contact Mechanics*, Cambridge University Press, Cambridge, 1985.
23 J. Dolbow and M. Gosz, *Mech. Mater.*, 1996, **23**, 311–321.
24 W. C. Oliver and G. M. Pharr, *J. Mater. Res.*, 1992, **7**, 1564–1583.
25 J. E. Jakes, C. R. Frihart, J. F. Beecher, R. J. Moon, P. J. Resto, Z. H. Melgarejo, O. M. Suarez, H. Baumgart, A. A. Elmustafa and D. S. Stone, *J. Mater. Res.*, 2009, **24**, 1016–1031.
26 J. E. Jakes and D. S. Stone, *Philos. Mag.*, 2010, DOI: 10.1080/14786435.2010.495360.
27 S.-H. Lee, S. Wang, G. M. Pharr and H. Xu, *Composites, Part A*, 2007, **38**, 1517–1524.
28 B. Oommen and K. J. Van Vliet, *Thin Solid Films*, 2006, **513**, 235–242.
29 Q. S. Zheng and D. X. Du, *J. Mech. Phys. Solids*, 2001, **49**, 2765–2788.
30 E. Stora, Q. C. He and B. Bary, *Cem. Concr. Res.*, 2006, **36**, 1330–1344.
31 F. Deng, Q. S. Zheng, L. F. Wang and C. W. Nan, *Appl. Phys. Lett.*, 2007, **90**, 021914.
32 F. Deng and Q. S. Zheng, *Appl. Phys. Lett.*, 2008, **92**, 071902.
33 F. Deng and K. J. Van Vliet, submitted.
34 R. Hill, *J. Mech. Phys. Solids*, 1965, **13**, 213–222.
35 Y. Maalej, L. Dormieux, J. Canou and J. C. Dupla, in *Advances in Geomaterials and Structure*, Tunisia, 3–5 May 2006, pp. 687–692.
36 J. D. Ferry, *Viscoelastic Properties of Polymers*, Wiley, New York, 1980.
37 G. Constantinides, K. S. R. Chandran, F.-J. Ulm and K. J. Van Vliet, *Mater. Sci. Eng., A*, 2006, **430**, 189–202.
38 G. Constantinides, E. C. C. M. Silva, G. S. Blackman and K. J. Van Vliet, *Nanotechnology*, 2007, **18**, 305503.
39 H. Buckle, *The Science of Hardness Testing and its Applications*, American Society for Metals, Metal Park, OH, 1973.
40 D. Goritz, H. Raab, J. Frohlich and P. G. Maier, *Rubber Chem. Technol.*, 1999, **72**, 929.
41 O. Dessewffy, *Rubber Chem. Technol.*, 1962, **35**, 611.